Article

An Integrated GNSS/MEMS Accelerometer System for Dynamic Structural Response Monitoring under Thunder Loading

Jian Wang [1,2,*]**, Xu Liu** [1]**, Fei Liu** [1,2]**, Cai Chen** [1] **and Yuyang Tang** [2]

[1] School of Geomatics and Urban Spatial Informatics, Beijing University of Civil Engineering and Architecture, Beijing 102616, China
[2] Research Center for Urban Big Data Applications, Beijing University of Civil Engineering and Architecture, Beijing 100044, China
[*] Correspondence: wangjian@bucea.edu.cn

Abstract: Dynamic response monitoring is of great significance for large engineering structural anomaly diagnosis and early warning. Although the global navigation satellite system (GNSS) has been widely used to measure the dynamic structural response, it has the limitation of a relatively low sampling rate. The micro-electro-mechanical system (MEMS) accelerometer has a high sampling frequency, but it belongs to the approaches of acceleration measurements as the absolute position is unavailable. Hence, in this paper, an integrated vibration monitoring system that includes a GNSS receiver and 3-axis MEMS accelerometers was developed to obtain the dynamic responses under the thunder loading. First, a new denoising algorithm for thunderstorm-induced vibration data was proposed based on variational mode decomposition (VMD) and the characteristics of white noise, and the low-frequency disturbance was separated from the GNSS displacement time series. Then, a power spectral density (PSD) analysis using data collected by the integrated system was carried out to extract low/high natural frequencies. Finally, field monitoring data collected at Huanghuacheng, Hefangkou, and Qilianguan in Beijing's Huairou District were used to validate the effectiveness of the integrated system and processing scheme. According to the results, the proposed integrated GNSS/MEMS accelerometer system can not only be used to detect thunder loading events, but also completely extract the natural frequency based on PSD analysis. The high natural frequencies detected from the accelerometer data of the four Great Wall monitoring stations excited by the thunderstorms are 42.12 Hz, 12.94 Hz, 12.58 Hz, and 5.95 Hz, respectively, while the low natural frequencies detected from the GNSS are 0.02 Hz, 0.019 Hz, 0.016 Hz, and 0.014 Hz, respectively. Moreover, thunderstorms can cause the Great Wall to vibrate with a maximum displacement of 14.3 cm.

Keywords: global navigation satellite system (GNSS); MEMS accelerometer; thunder loading; variational mode decomposition (VMD); power spectral density (PSD)

1. Introduction

Dynamic response monitoring plays an important role in large engineering structural anomaly diagnosis and early warning [1]. The monitoring system for dynamic structural response is responsible for data acquisition and processing using sensors installed on the top of large engineering structures, like high-rise buildings, suspension bridges, architectural buildings, and towers [2]. To detect accurate dynamic structural response under dynamic effects such as traffic vibrations [3], earthquakes [4], and thunderstorms [5], it is necessary to develop a reliable monitoring system.

With global, all-weather, and real-time monitoring capability, GNSS can be used as a suitable monitoring system for dynamic structural response monitoring and forecasting

[6]. However, it is limited by a relatively low sampling rate compared with alternative measurement techniques [7]. Moreover, the accuracy of GNSS is degraded in harsh environments due to the blockage of signals from satellites, atmosphere, multipath effect, etc. [8]. By contrast, MEMS accelerometers are widely adopted in monitoring dynamic responses of large structures for high sampling frequency and environmental stability. However, it is a relative acceleration measurement as the initial position is unavailable [9].

To make the most of the complementary characteristics of GNSS and MEMS accelerometers in monitoring dynamic structural responses, an integrated GNSS/MEMS accelerometer system is proposed to monitor dynamic structural responses [10,11]. Li et al. discovered that the data from RTK and accelerometers installed on a steel tower in Tokyo agreed with each other well, and the redundancy of the monitoring system therefore had been achieved [12]. Meng et al. achieved the dynamic deformation monitoring of the suspension footbridge, Wilford Bridge, by using an integrated GPS–accelerometer data processing technique [13]. Han et al. modified the GPS deformation data to extract the deformation information of the bridge by reconstructing the high-frequency component of displacement and low-frequency component of GPS through the acceleration and restoring of real structural dynamic responses of the bridge [14]. Zeng et al. developed an integrated GNSS strong seismograph combining accelerometer and GNSS data-processing methods [15]. Based on the shaking table test and real-time seismic signals, they proved that this integrated GNSS strong seismograph could be used in seismic real-time monitoring. To sum up, based on all the research, the integrated GNSS/accelerometer monitoring could effectively improve the accuracy of dynamic response monitoring.

From the above, the current research of large engineering structures under dynamic effects has focused mainly on traffic vibrations, earthquakes, wind and rain erosion, and so on. However, monitoring thunderstorm-induced vibrations for large engineering structures remains neglected [16,17]. The thunderstorm is also one of the main damaging factors to large engineering structures in Beijing during summer (in June, July, and August) annually [18]. It not only causes the foundations to shake, thus affecting the safety of large engineering structures, but also causes irreversible damage to the structures [19]. Therefore, it is significant to implement vibration monitoring for thunderstorm hazards, analyze the impact of thunderstorms on the stability of the structures, as well as explore the dynamic response characteristics of the structures.

The focus of this paper was to develop an integrated GNSS/MEMS accelerometer system to monitor the vibrations of the ancient Great Wall in Huairou District, Beijing. We first introduced a denoising algorithm based on VMD and the characteristics of white noise to eliminate the noise component from GNSS/accelerometer measurements. Secondly, an integrated spectral analysis based on PSD using low-frequency GNSS signals and high-frequency accelerometer signals was performed to extract natural frequencies excited by the thunder loading. Then, a software simulation test was carried out to verify the accuracy of the integrated spectral analysis. Finally, the effectiveness of the integrated data processing algorithm was evaluated with a field monitoring dataset collected by a self-developed GNSS/accelerometer combined monitoring system installed separately at three locations in the Huairou District of Beijing (Huanghuacheng, Hefangkou, and Qilianguan). The research results could help avoid the influence of thunderstorms and other natural disasters on the Great Wall, and further be applied in the protection of the Great Wall.

2. Methodology

2.1. A Denoising Algorithm Combined VMD with the Characteristics of White Noise

Variational mode decomposition (VMD) is widely used today to decompose the signal into different intrinsic mode functions (IMFs) from the high to low frequency bands. Typically, the natural noise dominates at high frequencies. Furthermore, the highest frequency IMF can be regarded as the high-frequency noise of the signal, while the lowest

frequency IMF represents the trend item or average value of the signal [20,21]. A roughly denoised function based on the VMD is obtained by removing the highest frequency IMF and the lowest frequency IMF as follows.

$$X = \sum_{i=1}^{N} IMF_i \tag{1}$$

$$X' = X - IMF_1 - IMF_N \tag{2}$$

where X means the reconstructed signal by VMD, N denotes the highest decomposition number, and X' is the denoised signal by "breaking off both ends". However, this method still fails to extract useful information accurately from the signals due to residual components of the useful signal in the *IMF* at the highest and lowest frequencies. Thus, it is necessary to select the quantitative criterion to separate useful signals, noises, and trend items. Flandrin et al. (2004) suggested that the product of energy density (E_n) of each IMF with Gaussian white noise and average period ($\bar{T}_n$) of the signal is a constant as follows [22]:

$$E_n \cdot \bar{T}_n = const \tag{3}$$

The energy density (E_n) is computed by Equation (4).

$$E_n = \frac{1}{N} \sum_{j=1}^{N} [IMF_n(j)]^2 \tag{4}$$

The average period ($\bar{T}_n$) is computed by Equation (5).

$$\bar{T}_n = \frac{N*2}{Count(Optima_n)} \tag{5}$$

where $Count(Optima_n)$ suggests the extremum number of IMF_n, and N refers to the total length of the signal [23].

The basic steps of the denoising algorithm combining VMD with the characteristics of white noise are as follows:

(1) Apply PSD to extract the frequency component of GNSS signals and determine the decomposition level n according to the number of spectrum peaks (the level is between five to eight empirically);

(2) Employ VMD to decompose the signal into different intrinsic mode functions (*IMFs*) from the high to low frequency bands, and extract the frequency of each *IMF* by PSD;

(3) Check whether the signal contains a trend item based on the frequency of each *IMF*. If yes, the reconstructed signal is computed as follows: $X = \sum_{i=1}^{N-1} IMF_i$. Otherwise, the reconstructed signal is constructed as follows: $X = \sum_{i=1}^{N} IMF_i$;

(4) Calculate the product of energy density (E_n) of each IMF with Gaussian white noise and average period ($\bar{T}_n$) of the signal;

(5) Detect the shift points of the product as denoised signals.

The flowchart of denoising algorithm combined VMD with the characteristics of white noise is summarized in Figure 1. as follows:
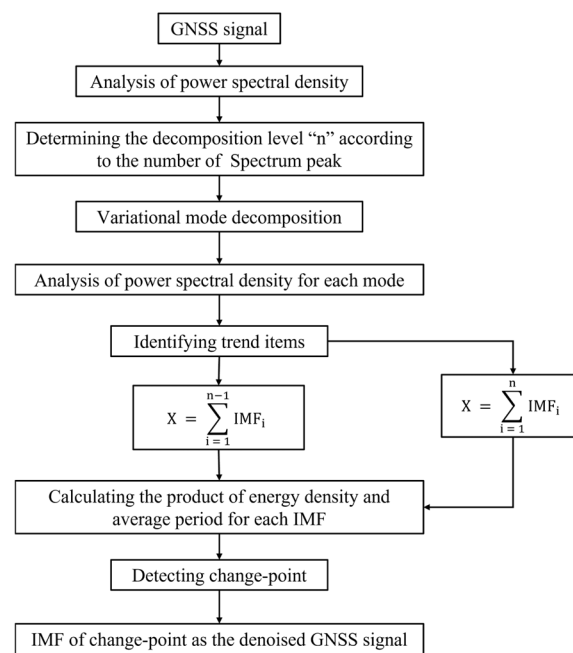
Figure 1. The flowchart of denoising algorithm combined VMD with the characteristics of white noise.

To verify the reliability of the denoising algorithm that combines VMD and the characteristics of white noise, MATLAB was used for simulation testing. A series of sinusoidal waves were simulated with a vibrational frequency of 0.1 Hz, a sampling frequency of 1 Hz, an amplitude of 10 mm, and a duration of 2 min. In addition, the effect of random noise was also added, with 0 mean value and 5 mm variance. Figure 2a gives the PSD curves for five IMFs using VMD. The dominant frequency is identified at about 0.1 Hz in IMF3 (see the red circle in Figure 2a), which is consistent with the true frequency of the simulated signal. Figure 2b shows five points that represent the product of energy density (E_n) of each IMF with Gaussian white noise and average period ($\bar{T}_n$) of the signal, along with the shift point at IMF3. Thus, IMF3, which contains the most useful component of the signal, could be regarded as the denoised signal.
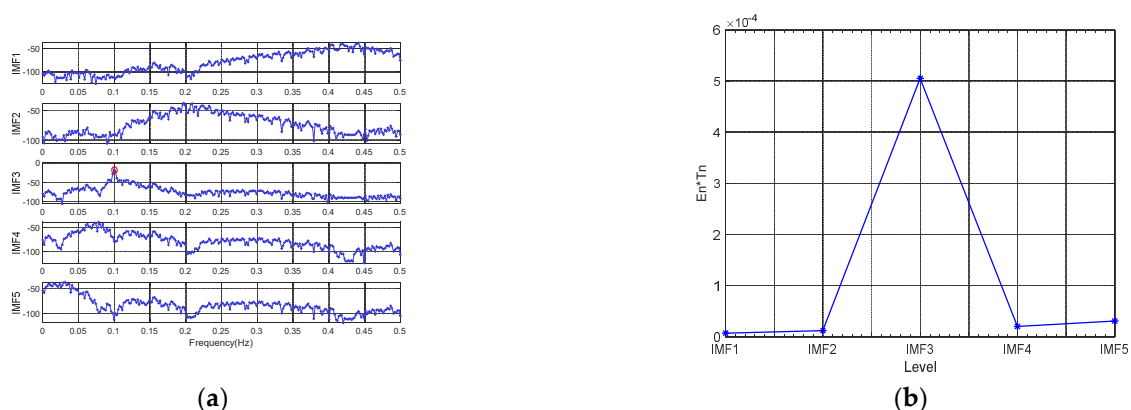

(**a**)

(**b**)

Figure 2. PSD curves and product of energy density and average period of each IMF: (**a**) PSD curves for five IMFs; (**b**) the curve of the product of energy density and average period.

Figure 3 illustrates the comparison between the simulated signal with the noise and the denoised signal. More specifically, the denoised signal is very close to the simulated real signal in terms of the setting parameters of frequency and amplitude. Therefore, both

the effectiveness and reliability of the denoising algorithm combining VMD with the characteristics of white noise are theoretically demonstrated.
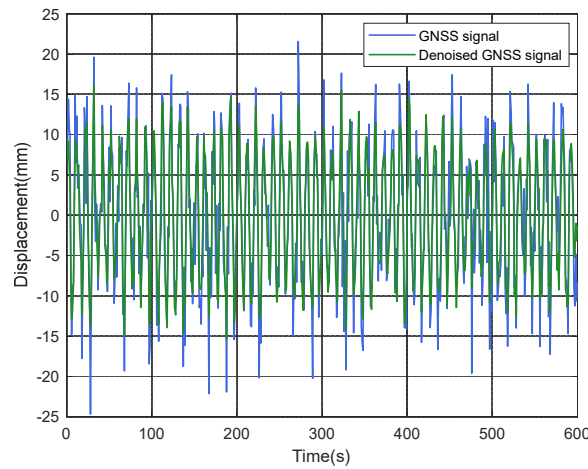

Figure 3. Comparison of simulated GNSS signal with noise and the denoised signal.

2.2. Power Spectral Density (PSD)

Power spectral density (PSD) is generally used to extract the dominant frequency of random signals, when random signals in the time or space domain are transformed to the temporal or frequency domain by the Fourier transform. The PSD curve characterizes power versus frequency, where its horizontal axis denotes the frequency (Hz) and the vertical axis means PSD (dB/HZ) [24]. The calculation proceeds as follows.

Compute the fast Fourier transform (FFT) of the random signal $x(n)$ as a series of finite energy. The FFT function is denoted by $X(k)$ and is given by

$$X(k) = \sum_{n=0}^{N-1} x(n)e^{-j2\pi kn/N} \tag{6}$$

where N suggests the number of acquisition points of $x(n)$, j is the imaginary number, and $k = 0, 1, \ldots, N-1$.

Take the modular square of amplitude of $X(k)$ and divide by "N" to get an estimate of the PSD. The formula for PSD can be expressed as follows.

$$S(k) = \frac{1}{N}|X(k)|^2 \tag{7}$$

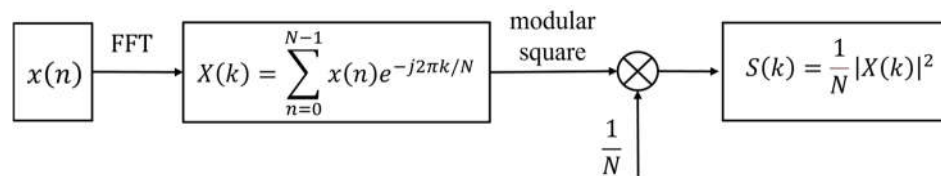The calculation flowchart is as follows (see Figure 4):

Figure 4. Flowchart of PSD calculation.

However, the above traditional PSD is not effective due to the large variance estimates. Furthermore, the variance does not decrease with the length of the $x(n)$ [25]. To solve this issue, the averaged periodogram (Welch's Method) is put forward as follows: first, the random signal is divided into segments with partial overlapping. Then, PSD for each segment is calculated. Finally, the average value of PSD is obtained.

The function of averaged periodogram is defined as:

$$S_{xx}(k) = \frac{1}{MN_{FFT}}\sum_{i=1}^{M} X_i(k)X_i^*(k) \tag{8}$$

where $X_i(k)$ means the Fourier transform of the i-th segment of a random signal, $X_i^*(k)$ is the conjugate plural of $X_i(k)$, and M indicates the average number of times.

To evaluate the effectiveness of the integrated method based on GNSS with accelerometer for structural natural frequency extraction, the GNSS and accelerometer signals are simulated using MATLAB. First, a set of analog signal waveforms simulates the real valued signal that consists of two sinusoidal signals with different frequencies (the frequencies are 0.1 Hz and 10 Hz, respectively) at a sampling frequency of 100 Hz, with an amplitude of 10 mm and a duration of 10 min. The expression of the real valued signal is as follows: $y = 0.01 \times \sin(2 \times pi \times 0.1 \times t) + 0.01 \times \sin(2 \times pi \times 10 \times t)$. Then, a random error with zero mean and a 5-mm variance is added to simulate the GNSS signal. To simulate the accelerometer signal, the real-valued signal is divided by the second-derivative method, and a random error with 1 m/s^2 is added. The simulated GNSS signal and the accelerometer signal are shown in Figure 5.
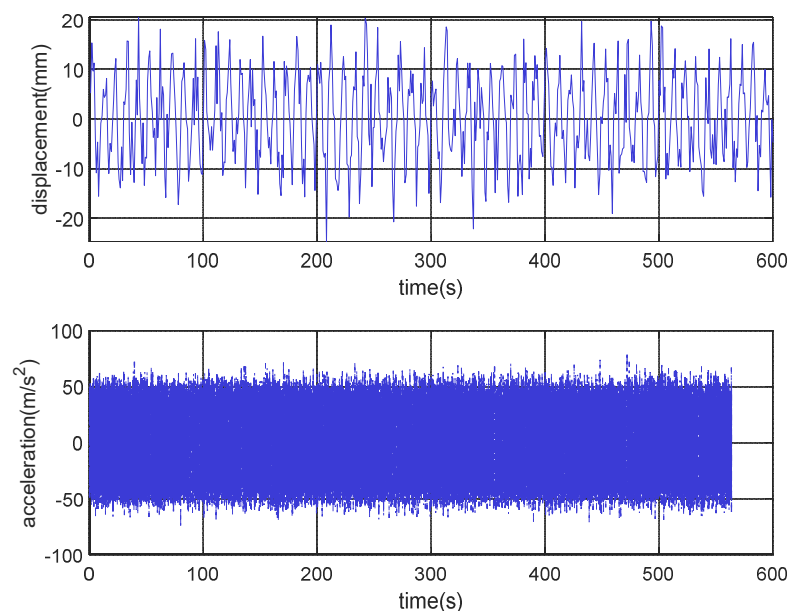

Figure 5. The simulated GNSS signal (**top**) and accelerometer signal (**bottom**).

Figure 6a displays a PSD curve for the simulated GNSS signal, where the extracted frequency ranges from 0.002 Hz to 0.5 Hz (the minimum frequency is the frequency resolution and the maximum frequency is half of the sampling frequency according to the Nyquist–Shannon sampling theorem), and the dominant frequency is detected at about 0.1 Hz. Figure 6b is a PSD curve for an analog accelerometer signal with a frequency extraction range of 0.2–50 Hz and a single peak value at 10 Hz. Evidently, GNSS can only detect low-frequency displacements in the frequency range, whereas accelerometers are capable of sensing high-frequency accelerations. The accelerometer cannot measure low-frequency accelerations even if the sampling frequency is lower than the low natural frequency, when its design has low noise at frequencies below the sampling frequency. Overall, the integrated method based on GNSS with accelerometers can fully extract the natural frequency of signals.
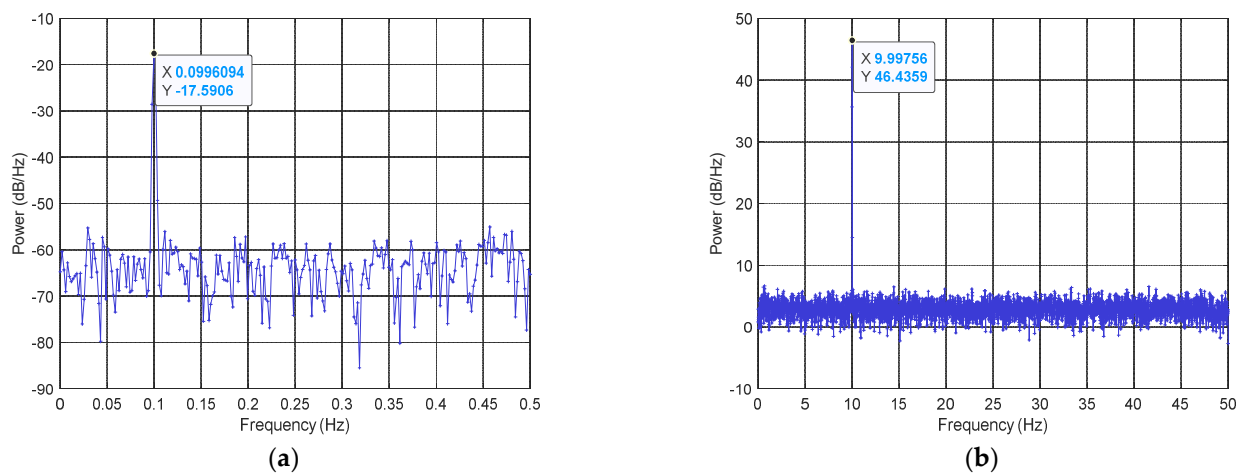
Figure 6. Comparison of frequency extracted by GNSS and accelerometer: (**a**) PSD for the simulated GNSS signal; (**b**) PSD for simulated accelerometer signal.

2.3. The Schematic to Detect Dynamic Responses Using an Integrated GNSS/MEMS Accelerometers System

A data processing flow combining GNSS and MEMS accelerometers was introduced to monitor thunder-induced dynamic responses of the Great Wall. First, the low-frequency noise component of the GNSS was removed by applying a denoising algorithm that combined VMD with the characteristics of white noise to accurately monitor thunder-induced displacement responses. Then, the power spectral density (PSD) was used to extract the low/high natural frequency using GNSS and accelerometers. Finally, a correlation analysis was performed to detect the relationship between acceleration time series, GNSS coordinate time series, and thunderstorm data. The flowchart of the dynamic response under thunder loading using GNSS and accelerometers is summarized in Figure 7. Purple represents the input data, blue-grey represents the output data, and orange represents the core approach.
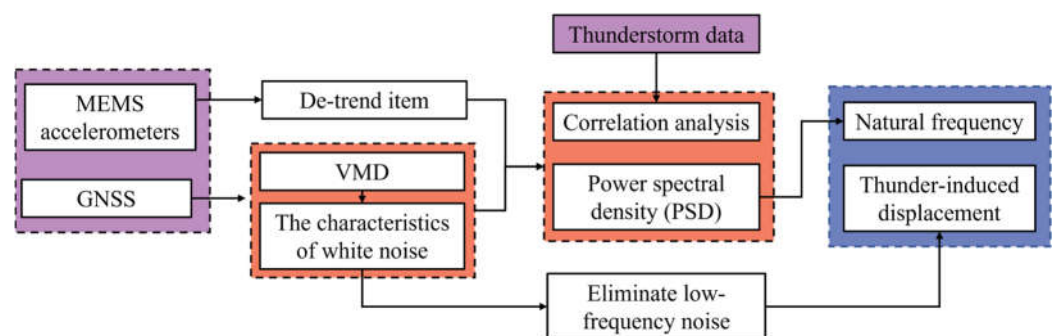

Figure 7. Flowchart for dynamic responses under thunder loading using GNSS and accelerometer.

3. The GNSS/Accelerometer Vibration Monitoring System

The GNSS/accelerometer vibration monitoring system was independently developed by the Beijing University of Civil Engineering and Architecture, and is mainly composed of five subsystems: a GNSS/accelerometer monitoring receiver (composed of SCA3300 series 3-axis MEMS accelerometers by Murata Manufacturing Co., Ltd. (Nagaokakyō, Japan) and GNSS board by Unicore Communications, Inc. (Beijing, China)), the GNSS antenna, the self-developed data processing system, the data transmission system, and a power supply (see Figure 8). The GNSS board at a sampling frequency of 1 Hz receives the satellite signal amplified by antennas and transmits it to the cloud server through TCP/IP protocol using 4G transmission antennas. Then, the server computes the satellite

raw data online and displays the deformation sequence in real time through cloud monitoring software to determine the satellite status and solution status. During the whole process, it is convenient to detect anomalies in a timely manner and take necessary measures to implement real-time displacement deformation monitoring and early warning at the millimeter level. Simultaneously, acceleration data are collected by a MEMS accelerometer at a sampling frequency of 100 Hz. The specifications of the system are given in Table 1. The hardware device is powered with solar energy, which can provide stable and sufficient power to the GNSS/accelerometer monitoring receiver.
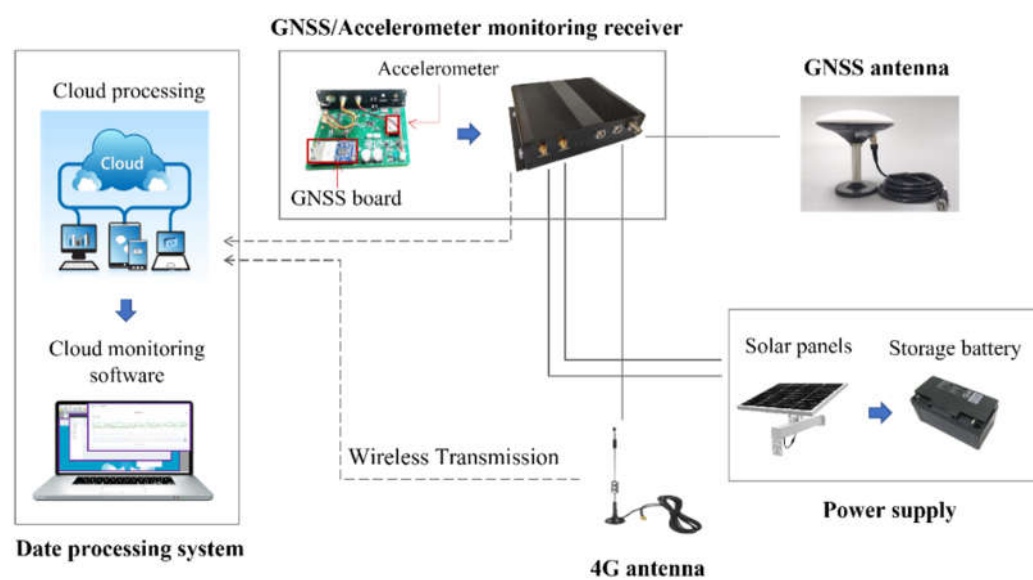

Figure 8. The GNSS/accelerometer vibration monitoring system.

Table 1. Principal specifications of GNSS and accelerometer.

Equipment	Performance	
GNSS	Signal tracking	BDS:B1/B2/B3; GPS: L1/L2/L5; GLONASS: L1/L2; GALILEO: E1/E5a/E5b; QZSS: L1/L5; SBAS: L1
	RTK(RMS)	Horizontal: ±8mm + 1 ppm; Vertical: ±15mm + 1 ppm
	Updating frequency	1 Hz
Accelerometer	Measurement range	6 g
	Noise density	37 $\mu g/\sqrt{Hz}$
	Offset error	1.15 mg
	Linearity error	1 mg
	Initial bias error (one year)	10 mg

4. Field Experiment

4.1. The Great Wall

The Great Wall of China, one of the architectural marvels, natural landscapes, and cultural heritages in human history, carries its outstanding universal value [26]. According to the survey results by the Great Wall Society of China, only about 8.2% of the Ming Great Wall is well preserved and 74.1% is poorly preserved due to the perennial impact of weathering and erosion, human destruction, earthquakes, thunderstorms, etc. [27] (see in Figure 9).

Figure 9. Deformation (**left**) and collapse (**right**) of the Great Wall.

4.2. Location of the Monitoring Points

The Great Wall in Beijing's Huairou district is about 63 km long and contains many famous attractions such as the Mutianyu Great Wall, Jiankou Great Wall, and Huanghuacheng Great Wall. In September 2021, a series of GNSS/accelerometer vibration monitoring systems were installed to collect GNSS (1 Hz) and accelerometer data (100 Hz) in three sections (namely, Erdaoguan Great Wall, Qiliankou Great Wall, and Hefangkou Great Wall, as suggested in Figure 10).
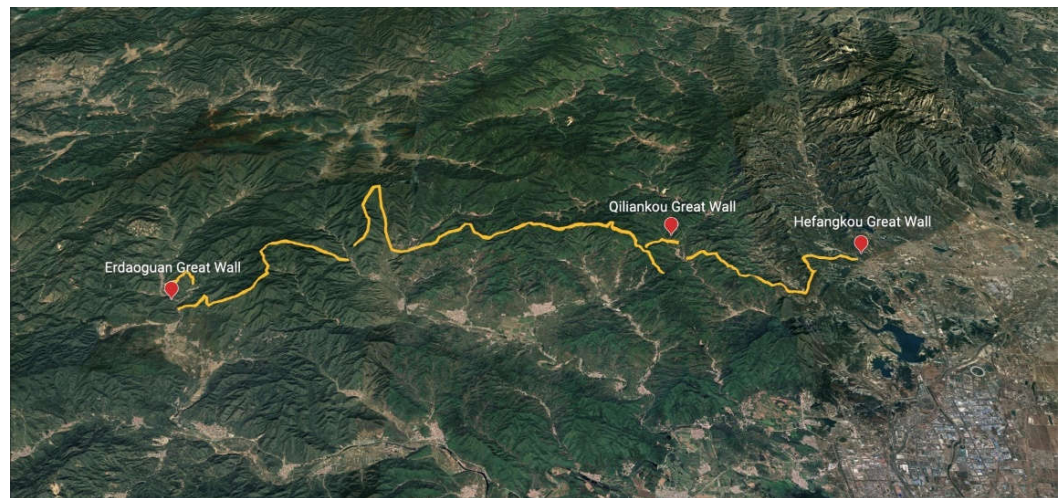

Figure 10. The Great Wall in the Huairou district.

Hefangkou Great Wall is located in the north of Huaibei Town, Huairou District, which is crossed by Jingjia Road. Qilianguan Great Wall is located in Lianchi Village, Yanqi Town, which is the first pass of Pond Road in Ji Town. Erdaoguan Great Wall is located in the Erdaoguan Village, near Ansi Road. The three sections of the Great Wall are not only affected by natural disasters, but also damaged by perennial traffic vibration. Even worse, the three sections lack repair and maintenance because they are the wild Great Wall. Therefore, these three sections are more severely damaged than the others (Figure 9). In total, two monitoring systems were installed at Erdaoguan Great Wall (see in Figure 11a), a monitoring system was installed at Qilianguan Great Wall (see in Figure 11b), and a monitoring system was installed at Hefangkou Great Wall (see in Figure 11c). The geographical locations of the monitoring systems are shown in Figure 11. Due to the biases from one monitoring system to another being unknown, we calibrated those monitoring systems to remove the bias by uniformly removing the mean value.

(**a**) Erdaoguan Great Wall   (**b**) Qiliankou Great Wall   (**c**) Hefangkou Great Wall

Figure 11. Deployment of the monitoring systems.

The equipment was installed in a non-destructive manner, with no holes drilled or walls knocked down to avoid damage to the wall's bricks. Steel plates customized and processed according to different thickness of walls were spliced into an "N" shape and attached to the wall. The installation of the equipment was performed on a customized steel plate, as illustrated in Figure 12.
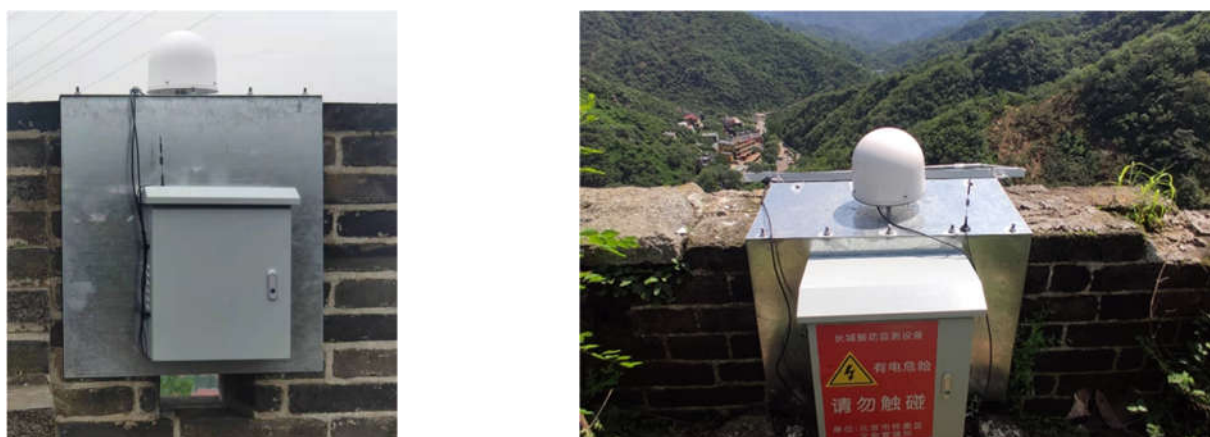

Figure 12. Equipment with non-destructive installation.

4.3. Meteorology Data

To evaluate the impacts of thunderstorm excitation on the stability of the Great Wall and measure vibration characteristic parameters (i.e., displacement and natural frequency), GNSS and accelerometer datasets were collected during two thunderstorm days (website for weather history: China Meteorological Data Service Centre https://data.cma.cn (accessed on 5 July 2022)) at four monitoring stations. The weather conditions for 5 July 2022 and 4 August 2022 are listed below in Table 2. Thunderstorms occurred on both days between 19:00 and 22:00, and there was no thunder, rain or wind on the rest of the two days.

Table 2. The weather conditions for 5 July 2022 and 4 August 2022 in Huairou, Beijing.

Beijing time	5 July 2022		4 August 2022	
	Weed Speed (m/s)	Severe Weather	Weed Speed (m/s)	Severe Weather
19:00	moderate breeze (6 m/s)		moderate breeze (7 m/s)	thunderstorm
19:30	gentle breeze (5 m/s)	(weak) thunderstorm, rain	gentle breeze (5 m/s)	(weak) thunderstorm, rain
20:00	light breeze (3 m/s)	(weak) thunderstorm, rain	light breeze (3 m/s)	(weak) thunderstorm, rain
20:30	light air (1 m/s)	(weak) thunderstorm, rain	light breeze (3 m/s)	thunderstorm, rain

21:00	light air (1 m/s)	(strong) thunder-storm	gentle breeze (4 m/s)	(weak) thunderstorm, gust, rain
21:30	light breeze (3 m/s)		light breeze (3 m/s)	thunderstorm
22:00	light air (1 m/s)		light breeze (2 m/s	

5. Results and Analysis

5.1. Analysis of Accelerometer Data

5.1.1. Accelerometer Data Collected on 5 July 2022

Figure 13 shows a set of vertical acceleration time series of the vibration frequencies from 100 Hz accelerometer data. The four monitoring stations were numbered 63, 64, 66, and 67 under 24-h thunder-induced vibration on July 5, 2022. The acceleration time series also changed greatly during almost the same period (72,000–75,600 s, 20:00–21:00 Beijing time), which corresponded with the occurrence of thunderstorms (see Table 2).
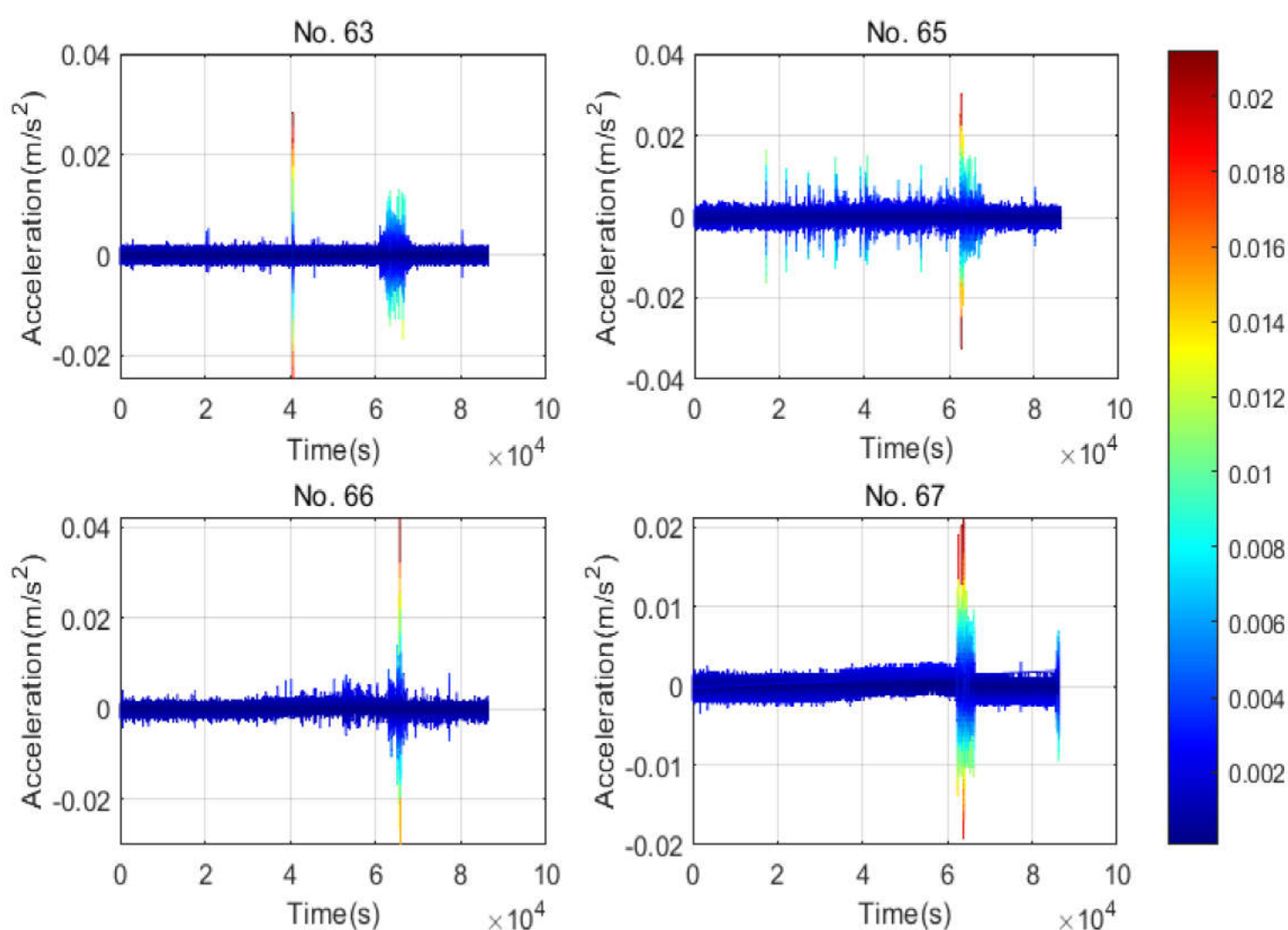

Figure 13. Acceleration time series for four monitoring stations on 5 July.

Figure 14 depicts the corresponding power of the above four sets of acceleration time series. The detected dominant frequency discrepancies were largely distributed among the four stations with 41.87 Hz, 11.74 Hz, 12.62 Hz, and 5.35 Hz, respectively.
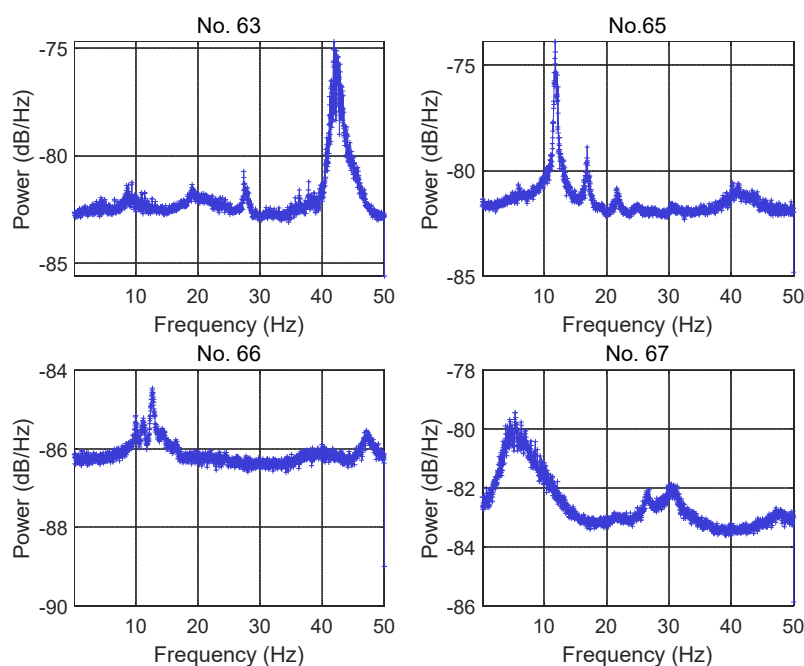
Figure 14. PSD curves for accelerometer data of the four stations on 5 July.

5.1.2. Accelerometer Data Collected on 4 August 2022

Figure 15 demonstrates the vertical acceleration time series of the vibrational frequencies obtained from the 100 Hz accelerometer data under thunder-induced vibration for 24 h. The acceleration time series of the four monitoring stations (No. 63/64/66/67) fluctuated significantly during almost the same period (68,400–77,400 s, 19:00–21:30 Beijing time). The maximum amplitude occurred at the 33,900 s (21:28 Beijing time), which was highly consistent with the time of the thunderstorm on 4 August 2022 (see Table 2). The analysis based on the two-day acceleration time series suggested that each monitoring station was affected by thunder-induced vibrations.
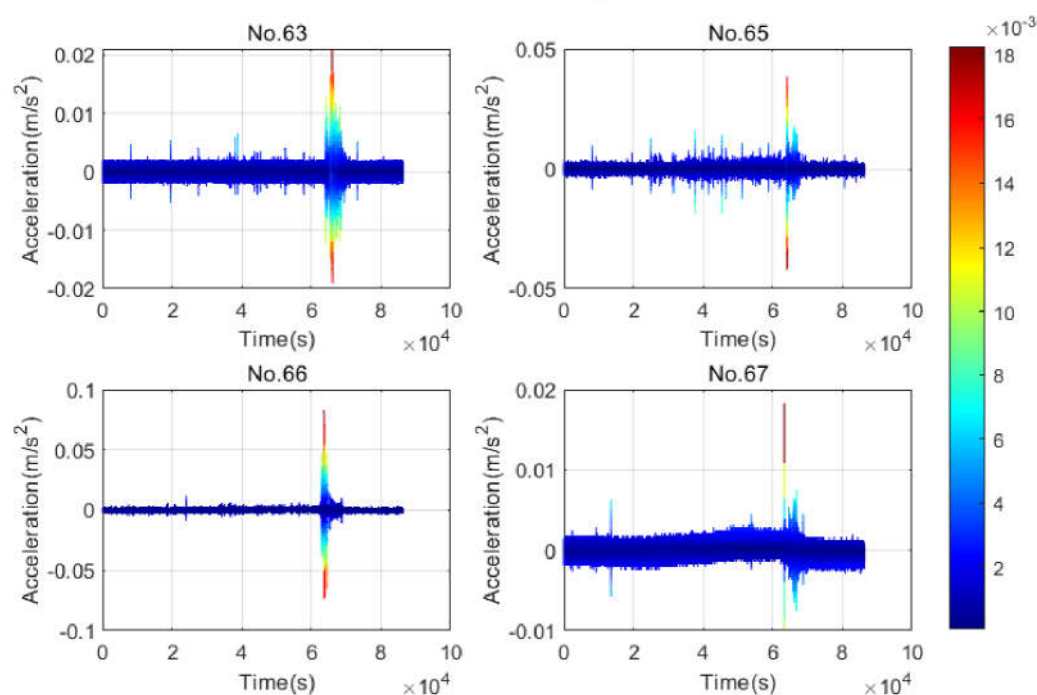

Figure 15. Acceleration time series for four monitoring stations on 4 August.

As can be seen from Figure 16, the dominant frequencies identified among the four stations based on the acceleration time series on 4 August were approximately 42.36 Hz, 14.11 Hz, 12.54 Hz, and 6.57 Hz, respectively.
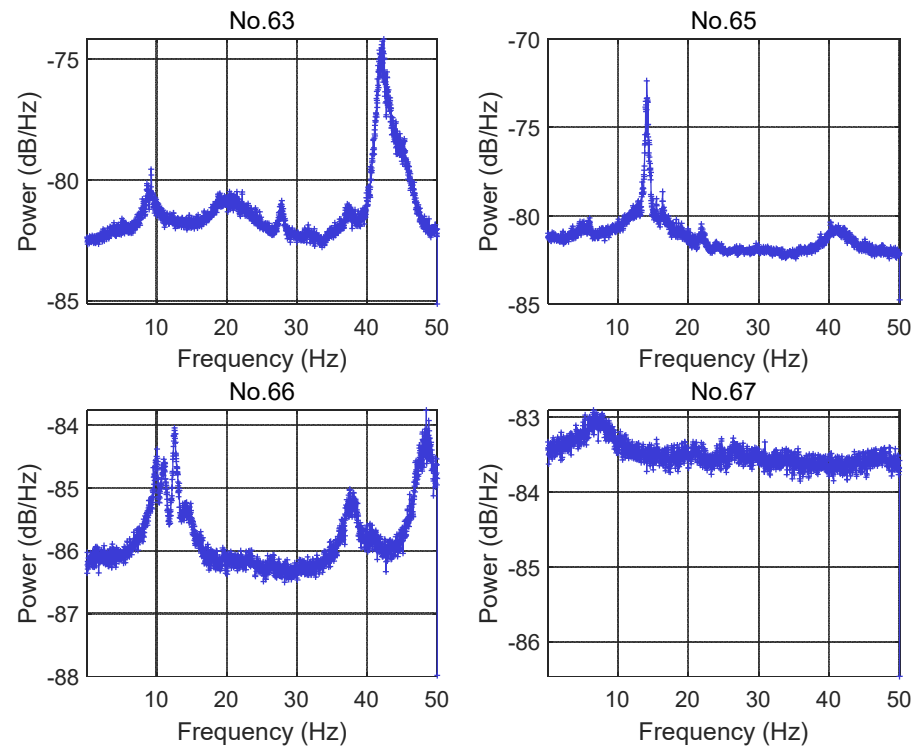

Figure 16. PSD curves for accelerometer data of the four stations on 4 August.

5.2. Analysis of GNSS Data

5.2.1. GNSS Data Collected on 5 July 2022

A similar analysis was applied to GNSS measurements collected from four monitoring stations on thunderstorm days. Figure 17 shows the vertical GNSS coordinate time series and the corresponding power spectra of the vibrational frequencies obtained from the 1 Hz GNSS data under 24-h thunder-induced vibrations on 5 July 2022. The GNSS coordinate time series of the four monitoring stations (No. 63/64/66/67) had a large displacement amplitude almost at the same period (72,000–75,600 s, 20:00–21:00 Beijing time), which was very close to the time of the thunderstorm on that day (see Table 2). The dominant frequencies identified among the four stations on August 4 were extremely close to 0.021 Hz, 0.019 Hz, 0.016 Hz, and 0.014 Hz, respectively (see Figure 18).
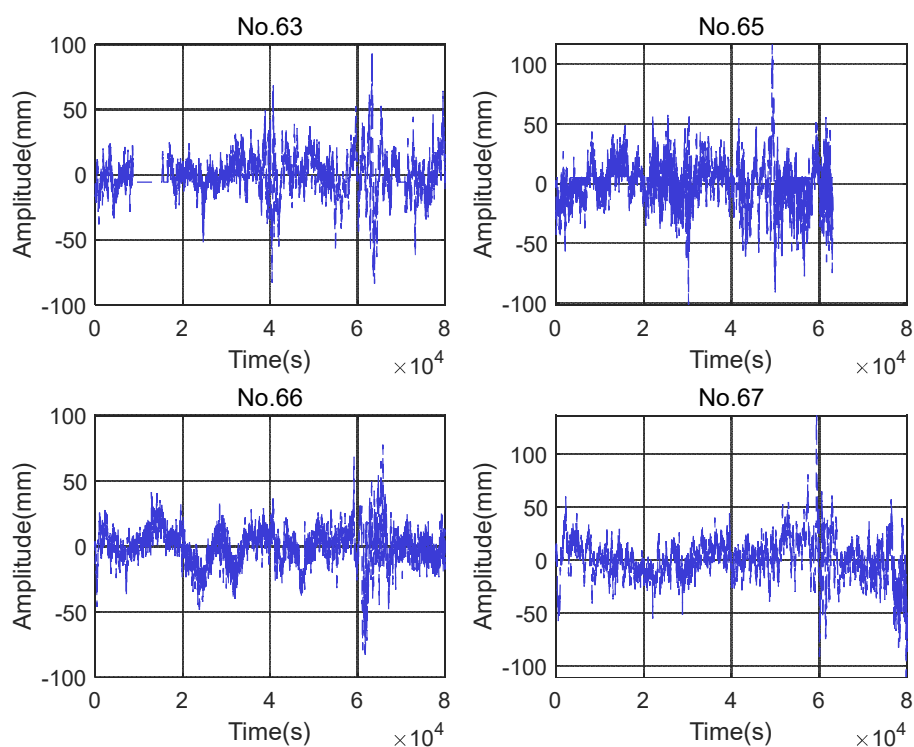
Figure 17. GNSS coordinate time series for four monitoring stations on 5 July.
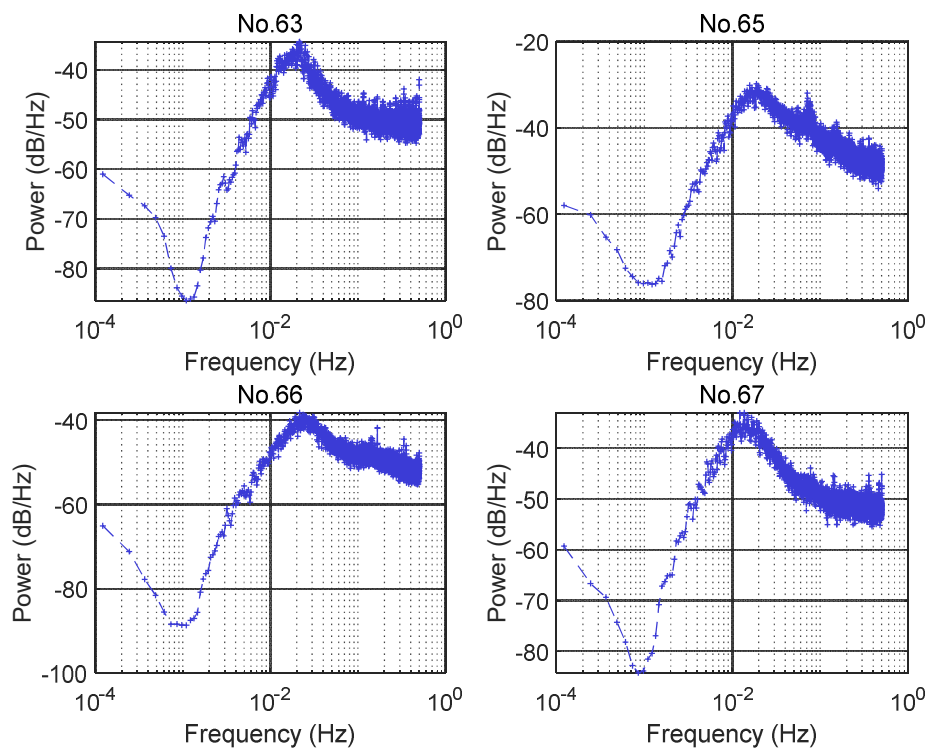

Figure 18. PSD curves for GNSS data of the four stations on 5 July.

5.2.2. GNSS Data Collected on 4 August 2022

The GNSS coordinate time series of the four monitoring stations (No. 63/64/66/67) fluctuated greatly during almost the same period (68,400–77,400 s, 19:00–21:30 Beijing

time). The maximum amplitude occurred in the 33,900s (21:28 Beijing time), which was highly consistent with the time of the thunderstorm on 4 August 2022 (see Table 2). Moreover, the large displacement amplitude of GNSS and accelerometer data occurred at the same time (see Figure 19). The detected frequencies among the four stations on August 4 were about 0.022 Hz, 0.019 Hz, 0.016 Hz, and 0.014 Hz, respectively (see Figure 20). Thus, the analysis based on two-day GNSS and accelerometer data suggests that each monitoring station of the Great Wall is affected by thunder-induced vibrations.
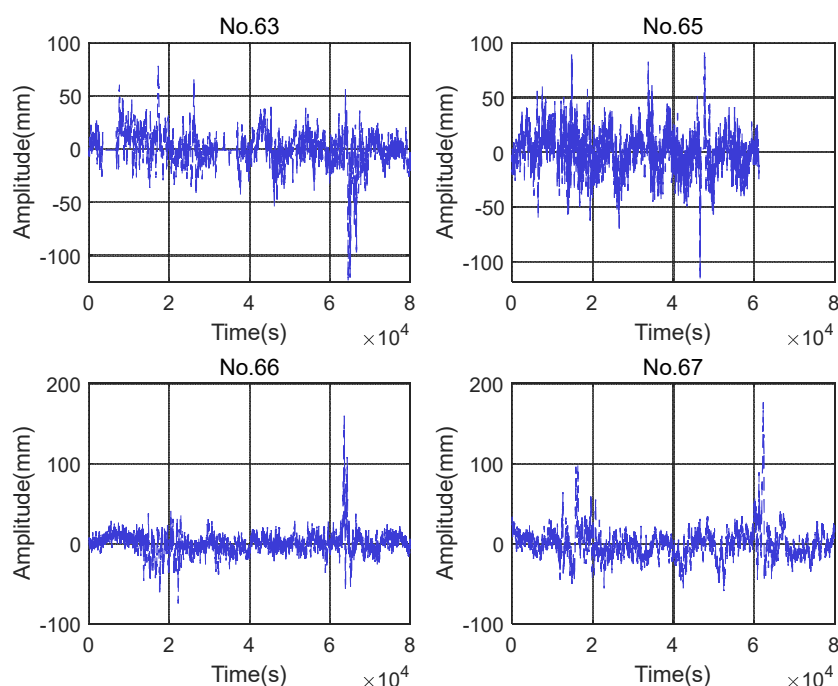

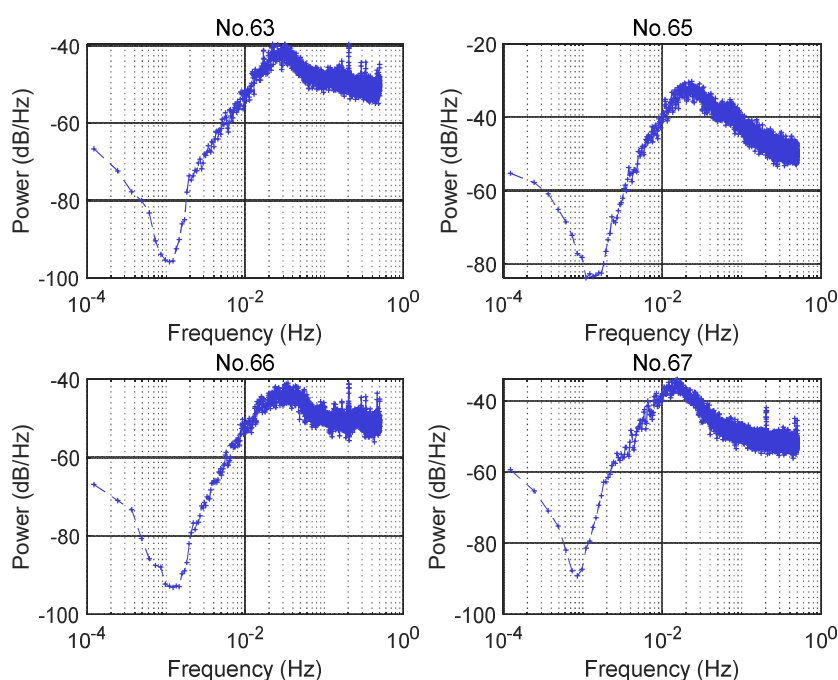**Figure 19.** GNSS coordinate time series for four monitoring stations on 4 August.

Figure 20. PSD curves for GNSS data of the four stations on 4 August.

5.3. Discussion

By comparing the two-day acceleration time series and GNSS coordinate time series, (see Table 3), the acceleration time series of the No.65 monitoring station on 5 July 2022 has a maximum value of 0.041 m/s^2, followed by 0.032 m/s^2 of the No.67 monitoring station, 0.021 m/s^2 of the No.66 monitoring station and 0.015 m/s^2 of the No.63 monitoring station. The GNSS coordinate time series at Station 65 has a maximum value of 140 mm, followed by 110 mm at Station 67, 90 mm at Station 66, and 80 mm at Station 63. It can be found that the magnitudes of maximum accelerations measured by the accelerometers of the four stations are of the same order as the magnitudes of the maximum displacements measured by the GNSS, which is in good agreement with the analysis on August 4.

The frequency of each station detected by GNSS on 5 July is close to that on 4 August. To obtain more accurate and unique natural frequencies detected from GNSS data, the natural frequencies of stations 63, 65, 66, and 67 can be calculated at 0.022 Hz, 0.019 Hz, 0.016 Hz, and 0.014 Hz, respectively, after averaging the frequencies of each station over two days.

Table 3. Displacements and frequencies extracted from GNSS and accelerometer measurements.

| Data | 20220705 | | | | 20220804 | | | |
| Equipment | Accelerometer | | GNSS | | Accelerometer | | GNSS | |
Station	Max acc/m/s^2	Freq/Hz	Max amp	Freq/Hz	Max acc/m/s^2	Freq/Hz	Max amp	Freq/Hz
No.63	0.015	41.87	80	0.021	0.021	42.36	110	0.022
No.65	0.041	11.74	140	0.019	0.017	14.11	120	0.019
No.66	0.021	12.62	90	0.016	0.081	12.54	180	0.016
No.67	0.032	5.35	110	0.014	0.041	6.57	160	0.014
Mean	0.027	/	105	/	0.040		143	

To sum up, the proposed integrated GNSS/MEMS accelerometer system can be used to detect thunder loading events. The above monitoring results demonstrate that thunderstorms can cause the Great Wall to vibrate. On 5 July 2022, the No.65 monitoring station was largely influenced by thunderstorms with a maximum displacement of 140 mm, followed by a 110-mm displacement of the No.67 monitoring station, a 90-mm displacement of the No.66 monitoring station, and an 80-mm displacement of the No.63 monitoring station. On 4 August 2022, Station 66 was heavily affected by thunderstorms, with a maximum displacement of 180 mm, followed by a 160 mm displacement of Station 67, a 120 mm displacement of Station 65, and a 110 mm displacement of Station 63. Compared with 5 July 2022 with a maximum displacement of 105 mm, the Great Wall suffered more damage by thunderstorms on 4 August 2022, with a mean displacement of 143 mm.

Moreover, the integrated GNSS/MEMS accelerometer system can fully extract the natural frequency based on PSD analysis. The natural frequencies of the four monitoring stations of the Great Wall, detected from the accelerometer data excited by thunderstorms, were 42.12 Hz, 12.94 Hz, 12.58 Hz, and 5.95 Hz, respectively. However, the natural frequencies of the four monitoring stations detected from the GNSS were 0.02 Hz, 0.019 Hz, 0.016 Hz, and 0.014 Hz, respectively, which are other possible natural frequencies.

6. Conclusions

In this paper, a series of GNSS/accelerometer integrated vibration monitoring systems are applied to monitor the vibrations of the ancient Great Wall in Huairou District, Beijing. Furthermore, a dynamic response detection approach consisting of VMD and PSD is proposed. In this regard, field tests were conducted on thunderstorm weather at four monitoring stations on the Great Wall. The conclusions are as follows.

(1) The integrated GNSS/MEMS accelerometer system for dynamic structural response monitoring can not only used to detect thunder loading events, but also fully extract the low/high natural frequency based on the data processing approach consisting of

VMD and PSD. The natural frequencies of the four monitoring stations of the Great Wall, detected from the accelerometer data excited by thunderstorms, were 42.12 Hz, 12.94 Hz, 12.58 Hz, and 5.95 Hz, respectively. However, the natural frequencies of the four monitoring stations detected from the GNSS were 0.02 Hz, 0.019 Hz, 0.016 Hz, and 0.014 Hz, respectively, which are other possible natural frequencies.

(2) Thunderstorms act as a dangerous factor affecting the stability of the Great Wall by exciting it into vibration, resulting in increased vibration displacements. On 4 August 2022, Station 66 was heavily affected by thunderstorms, with a maximum displacement of 180 mm, followed by displacements of 160 mm of Station 67, 120 mm of Station 65, and 110 mm of Station 63. Compared with a maximum displacement of 105 mm on 5 July 2022, the Great Wall suffered more damage by thunderstorms on 4 August 2022, with a mean displacement of 143 mm.

Currently, only a few integrated GNSS/MEMS accelerometer systems have been installed on the Great Wall. To obtain a reliable threshold level for the frequency of possible dynamic responses of the Great Wall, we will add more monitoring points for large-scale and long-term monitoring in future work.

Author Contributions: Conceptualization, J.W. and X.L.; methodology, X.L.; validation, J.W. X.L. and F.L.; investigation, X.L.; resources, J.W. and F.L.; data curation, F.L.; writing—original draft preparation, X.L.; writing—review and editing, J.W., X.L., F.L., C.C. and Y.T.; funding acquisition, J.W. and F.L. All authors have read and agreed to the published version of the manuscript.

Data Availability Statement: The data presented in this study are available on request from the corresponding author.

Conflicts of Interest: The authors declare no conflict of interest.

References

1. Shen, N.; Chen, L.; Liu, J.; Wang, L.; Tao, T.; Wu, D.; Chen, R. A Review of Global Navigation Satellite System (GNSS)-Based Dynamic Monitoring Technologies for Structural Health Monitoring. *Remote Sens.* **2019**, *11*, 1001. https://doi.org/10.3390/rs11091001.
2. Xi, R.; Jiang, W.; Meng, X.; Chen, H.; Chen, Q. Bridge monitoring using BDS-RTK and GPS-RTK techniques. *Measurement* **2018**, *120*, 128–139.
3. Du, H.; Chen, X.; Wang, D.K. Analysis and Evaluation of the Impact of Vehicle Driving Vibration on the Ancient Great Wall. *J. Earthq. Eng.* **2019**, *41*, 1448–1453.
4. Tu, R.; Zhang, R.; Zhang, P.; Liu, J.; Lu, X. Integration of Single-Frequency GNSS and Strong-Motion Observations for Real-Time Earthquake Monitoring. *Remote Sens.* **2018**, *10*, 886. https://doi.org/10.3390/rs10060886.
5. Guerova, G.; Dimitrova, T.; Georgiev, S. Thunderstorm Classification Functions Based on Instability Indices and GNSS IWV for the Sofia Plain. *Remote Sens.* **2019**, *11*, 2988. https://doi.org/10.3390/rs11242988.
6. Qu, X.; Shu, B.; Ding, X.; Lu, Y.; Li, G.; Wang, L. Experimental Study of Accuracy of High-Rate GNSS in Context of Structural Health Monitoring. *Remote Sens.* **2022**, *14*, 4989. https://doi.org/10.3390/rs14194989.
7. Xu, P.; Shi, C.; Fang, R. High-rate precise point positioning (PPP) to measure seismic wave motions: An experimental comparison of GPS PPP with inertial measurement units. *J. Geod.* **2013**, *87*, 361–372.
8. Liu, X.; Wang, J.; Zhen, J.; Han, H.; Hancock, C. GNSS-aided accelerometer frequency domain integration approach to monitor structural dynamic displacements. *Int. J. Image Data Fusion* **2021**, *12*, 268–281.
9. Lin, J.-F.; Li, X.-Y.; Wang, J.; Wang, L.-X.; Hu, X.-X.; Liu, J.-X. Study of Building Safety Monitoring by Using Cost-Effective MEMS Accelerometers for Rapid After-Earthquake Assessment with Missing Data. *Sensors* **2021**, *21*, 7327. https://doi.org/10.3390/s21217327.

10. Meng, X.; Dodson, A.H.; Roberts, G.W. Detecting bridge dynamics with GPS and triaxial accelerometers. *Eng. Struct.* **2007**, *29*, 3178–3184.
11. Sun, A.; Zhang, Q.; Yu, Z.; Meng, X.; Liu, X.; Zhang, Y.; Xie, Y. A Novel Slow-Growing Gross Error Detection Method for GNSS/Accelerometer Integrated Deformation Monitoring Based on State Domain Consistency Theory. *Remote Sens.* **2022**, *14*, 4758. https://doi.org/10.3390/rs14194758.
12. Li, X.; Ge, L.; Ambikairajah, E.; Rizos, C.; Tamura, Y.; Yoshida, A. Full-scale structural monitoring using an integrated GPS and accelerometer system. *GPS Solut.* **2006**, *10*, 233–247.
13. Meng, X.; Nguyen, D.T.; Owen, J.S.; Xie, Y.; Psimoulis, P.; Ye, G. Application of GeoSHM System in Monitoring Extreme Wind Events at the Forth Road Bridge. *Remote Sens.* **2019**, *11*, 2799. https://doi.org/10.3390/rs11232799.
14. Han, H.; Wang, J.; Meng, X.; Liu, H. Analysis of the dynamic response of a long span bridge using GPS/accelerometer/anemometer under typhoon loading. *Eng. Struct.* **2016**, *122*, 238–250.
15. Zeng, R.; Geng, J.; Xin, S.M. SMAG2000: Integrated GNSS strong seismograph and analysis of its seismic monitoring performance. *Geomat. Inf. Sci. Wuhan Univ.* **2020**, 1–12. https://doi.org/10.13203/j.whugis20200426.
16. Solari, G. Thunderstorm response spectrum technique: Theory and applications. *Eng. Struct.* **2016**, *108*, 28–46.
17. Roncallo, L.; Solari, G.; Muscolino, G.; Tubino, F. Maximum dynamic response of linear elastic SDOF systems based on an evolutionary spectral model for thunderstorm outflows. *J. Wind. Eng. Ind. Aerodyn.* **2022**, *224*, 104978.
18. Wang, Y.; Lu, G.; Shi, T.; Ma, M.; Zhu, B.; Liu, D.; Peng, C.; Wang, Y. Enhancement of Cloud-to-Ground Lightning Activity Caused by the Urban Effect: A Case Study in the Beijing Metropolitan Area. *Remote Sens.* **2021**, *13*, 1228. https://doi.org/10.3390/rs13071228.
19. Solari, G.; De Gaetano, P. Dynamic response of structures to thunderstorm outflows: Response spectrum technique vs time-domain analysis. *Eng. Struct.* **2018**, *176*, 188–207.
20. Dragomiretskiy, K.; Zosso, D. Variational mode decomposition. *IEEE Trans. Signal Process.* **2014**, *62*, 531–544.
21. Wang, J.; Liu, X.; Li, W.; Liu, F.; Hancock, C. Time–frequency extraction model based on variational mode decomposition and Hilbert–Huang transform for offshore oil platforms using MIMU data. *Symmetry* **2021**, *13*, 1443.
22. Flandrin, P.; Rilling, G.; Goncalves, P. Empirical mode decomposition as a filter bank. *IEEE Signal Process. Lett.* **2004**, *11*, 112–114.
23. Luo, Y.; Huang, C.; Zhang, J. Denoising method of deformation monitoring data based on variational mode decomposition. *Geomat. Inf. Sci. Wuhan Univ.* **2020**, *45*, 784–791.
24. Yang, C.H.; Wu, T.C. Vibration measurement method of a string in transversal motion by using a PSD. *Sensors* **2017**, *17*, 1643.
25. Wang, J.; Hu, X. *Application of MATLAB in Vibration Signal Processing*; China Water and Power Press: Beijing, China, 2006.
26. Li, Z.; Dong, Y.; Hou, M.; Wang, J.; Xin, T. Basic issues and research directions of the digital restoration of the Great Wall. *Natl. Remote Sens. Bull.* **2021**, *25*, 2365–238.
27. Available online: http://www.gov.cn/jrzg/2012-06/05/content_2153854.htm (accessed on 5 July 2022).